JUPITER'S DEEP CLOUD STRUCTURE REVEALED USING KECK OBSERVATIONS OF SPECTRALLY RESOLVED LINE SHAPES

G. L. Bjoraker[1], M. H. Wong[2], I. de Pater[2], and M. Ádámkovics[2]
[1] NASA/GSFC Code 693, Greenbelt, MD 20771, USA; gordon.l.bjoraker@nasa.gov
[2] Department of Astronomy, University of California, Berkeley, CA 94720-3411, USA

ABSTRACT

Technique: We present a method to determine the pressure at which significant cloud opacity is present between 2 and 6 bars on Jupiter. We use (a) the strength of a Fraunhofer absorption line in a zone to determine the ratio of reflected sunlight to thermal emission, and (b) pressure-broadened line profiles of deuterated methane (CH_3D) at 4.66 μm to determine the location of clouds. We use radiative transfer models to constrain the altitude region of both the solar and thermal components of Jupiter's 5 μm spectrum. *Results:* For nearly all latitudes on Jupiter the thermal component is large enough to constrain the deep cloud structure even when upper clouds are present. We find that hot spots, belts, and high latitudes have broader line profiles than do zones. Radiative transfer models show that hot spots in the North Equatorial Belt and South Equatorial Belt (SEB) typically do not have opaque clouds at pressures greater than 2 bars. The South Tropical Zone (STZ) at 32°S has an opaque cloud top between 4 and 5 bars. From thermochemical models this must be a water cloud. We measured the variation of the equivalent width of CH_3D with latitude for comparison with Jupiter's belt-zone structure. We also constrained the vertical profile of H_2O in an SEB hot spot and in the STZ. The hot spot is very dry for $P < 4.5$ bars and then follows the H_2O profile observed by the Galileo Probe. The STZ has a saturated H_2O profile above its cloud top between 4 and 5 bars.

Key words: planets and satellites: atmospheres – planets and satellites: gaseous planets – planets and satellites: individual (Jupiter)

1. INTRODUCTION

The abundance of H_2O in Jupiter's atmosphere is of fundamental importance in understanding the origin of Jupiter, the composition of its clouds, and Jovian dynamics beneath the upper cloud layers. Water was first detected on Jupiter by Larson et al. (1975) using the Kuiper Airborne Observatory (KAO). Bjoraker et al. (1986a, 1986b) analyzed both KAO and *Voyager IRIS* spectra in Jupiter's 5 μm spectral window to the deep atmosphere, finding a deep water abundance highly depleted with respect to the solar abundance. The spectrum between 4.5 and 5.4 μm provides a wealth of information about the gas composition and cloud structure of the troposphere of this giant planet. Jupiter's 5 μm spectrum is a mixture of scattered sunlight and thermal emission that changes significantly between belts and zones. Jupiter exhibits remarkable spatial structure at 5 μm. Chemical models of Jupiter's cloud structure predict three distinct layers: an NH_3 ice cloud near 0.5 bars, an NH_4SH cloud formed from a reaction of NH_3 and H_2S at 2 bars, and a massive water ice/liquid solution cloud near 5 or 6 bars, depending on assumptions of composition and thermal structure (see Weidenschilling & Lewis 1973 and Wong et al. 2015). Thermal emission from the deep atmosphere is attenuated by the variable opacity of one or more of these three cloud layers. Hot spots, located primarily in the North and South Equatorial Belts (NEB, SEB), exhibit 5 μm radiances up to 70 times larger than surrounding regions due to a minimum of cloud opacity. They also appear brighter than their surroundings at microwave wavelengths due to a low ammonia abundance (Sault et al. 2004).

The interpretation of 5 μm spectra of Jupiter, and the H_2O abundance in particular, has been hampered by uncertainties in the pressure level of the lower boundary of the emitting region. Two different models have been proposed. Bjoraker et al.

(1986a, 1986b) suggested that thermal radiation at 5 μm originates from levels as deep as 8 bars, 310 K where unit optical depth in H_2 occurs. In contrast, Carlson et al. (1992) proposed a model in which a massive water–ice cloud establishes the lower boundary near 5 bars, 273 K. Bjoraker et al. fitted KAO and *Voyager IRIS* spectra of H_2O in Jupiter's hot spots with a small abundance (4–30 ppm) distributed along a long path (60 km) between 2 and 8 bars. They also measured H_2O abundances in the low-flux zone regions using Voyager spectra. The NEB hot spots were found to be depleted in H_2O between 2 and 4 bars, but belts, zones, and hot spots could all be fitted by the same H_2O profile (4–30 ppm) between 4 and 8 bars. In marked contrast, Carlson et al. fitted Voyager hot-spot spectra using a much larger mixing ratio (up to 3000 ppm, equivalent to 3× the solar O/H measured by Asplund et al. 2009) confined to a narrow layer (10 km) between 4 and 5 bars immediately above an opaque water cloud. Carlson et al. also examined Voyager spectra of the Equatorial Zone (EQZ) and other regions away from hot spots. All regions required a saturated H_2O profile that increased from 300 ppm at 4 bars to 3000 ppm at 5 bars, although NEB hot spots were sub-saturated in the 2–4 bar region.

The Galileo Probe measured water vapor in situ at a single location on Jupiter, but unanswered questions remain about its global abundance. The probe entered Jupiter's atmosphere at 6.5°N planetocentric latitude near the southern portion of an NEB hot spot. The Galileo Probe Mass Spectrometer (Niemann et al. 1992) found water increasing with depth, from an upper limit of 0.8 ppm at 2.7 bar, to measured mole fractions of 40 ± 13 ppm at 11.0–11.7 bar and 420 ± 140 ppm at 18–21 bar (Niemann et al. 1998 and Wong et al. 2004b). The deepest value corresponds to 0.45× solar O/H. Ground-based imaging has shown that 5 μm hot spots, such as the one entered by the

Galileo probe, cover less than 1% of the surface area of Jupiter (Orton et al. 1996). Thus, the H_2O abundances observed by the probe may be characteristic of all or most hot spots, but they are probably not representative of Jupiter as a whole, especially since a range of other indirect studies (lightning flash depths, the tropospheric CO abundance, and discrete clouds at $P \geqslant 4$ bar) point to solar or supersolar water abundances (Wong et al. 2008). Since the Galileo probe found that carbon, sulfur, and nitrogen were enriched by $\sim 4 \times$ solar (Wong et al. 2004b), oxygen may also be enhanced by the same amount. Some formation models require $\sim 10 \times$ solar O/H in order to trap Jupiter's volatiles inside cages of water ice clathrates (Hersant et al. 2004). The Juno mission, scheduled to begin orbiting Jupiter in 2016 July, should answer many of these questions. The Microwave Radiometer will measure water vapor below Jupiter's clouds to determine the O/H ratio (Janssen et al. 2005). Interpretation of these data may not be straightforward, however, due to e.g., the small microwave absorptivity of H_2O gas compared with NH_3 (see de Pater et al. 2005 for details). A complementary way to determine the deep H_2O abundance, therefore, is highly desirable. The Jovian Infrared Auroral Mapper (JIRAM) will acquire near-infrared spectra of Jupiter, including the $5\,\mu m$ window (Adriani et al. 2014).

Water ice has been detected in isolated regions where active convection lofted the ice well above its condensation level (Simon-Miller et al. 2000), but water clouds are generally hidden by overlying NH_3 and NH_4SH clouds (e.g., Sromovsky & Fry 2010). Only very thin clouds were found in the Galileo Probe hot spot (Ragent et al. 1998), consistent with condensation via weak turbulent updrafts within the descending branch of an equatorially trapped Rossby wave (Friedson 2005; Wong et al. 2015). Models of NIMS spectra by Nixon et al. (2001) include water clouds in at least some hot spots, and Roos-Serote et al. (2004) showed that NIMS spectra of hot spots cannot rule out water clouds whose opacity is entirely restricted to $P > 5$ bar. Evidence for water clouds in Jupiter's zones is also ambiguous. Drossart et al. (1998) compared dayside and nightside NIMS spectra of low-flux regions in the EQZ. A saturated H_2O profile above an opaque water cloud at 5 bars provides a satisfactory fit to these data. At the spectral resolution of *IRIS* ($4.3\,\mathrm{cm}^{-1}$) and NIMS ($10\,\mathrm{cm}^{-1}$) we can only retrieve a column abundance of H_2O above an assumed lower boundary, which can be either a water cloud or opacity due to H_2. Thus, we simply cannot tell whether or not hot spots or zones have water clouds. This problem will also affect the interpretation of $5\,\mu m$ spectra from JIRAM on Juno, which has the same spectral resolution as *Voyager*/*IRIS* (Adriani et al. 2014).

In Section 2 we present ground-based observations of Jupiter's belts and zones that have sufficient spectral resolution to resolve line shapes. We demonstrate that we can derive the cloud structure at $P > 2$ bars even when higher-altitude clouds greatly attenuate the thermal flux from the deep atmosphere. We used line shapes to detect water clouds and to determine the pressure at which these clouds become optically thick. This resolves the ambiguity of whether the lower boundary of the $5\,\mu m$ line formation region is due to H_2 or due to opaque clouds. This, in turn, will yield more accurate gas abundances for use in constraining models of Jupiter's origin and in understanding the dynamics of the atmosphere beneath the upper clouds.
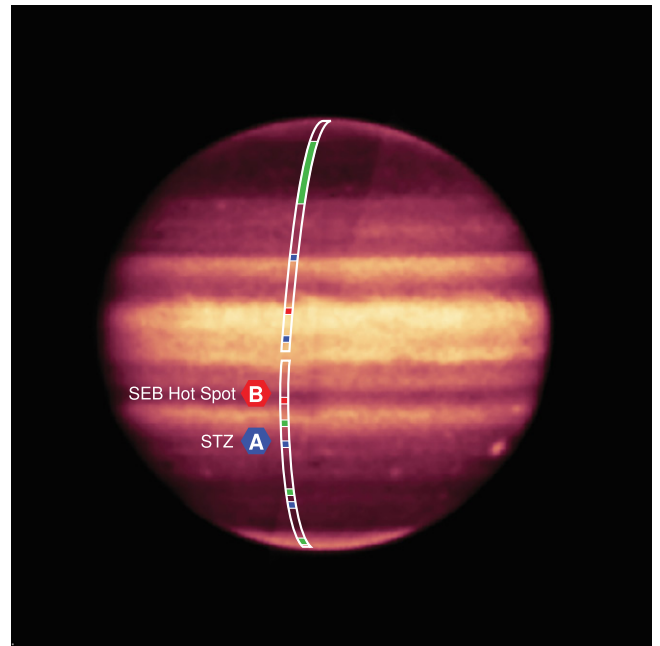
Figure 1. Keck/SCAM image of Jupiter at $2.12\,\mu m$ shows 2 NIRSPEC slit positions, one in the northern, and one in the southern hemisphere. Curvature is due to navigating positions onto an image taken a few minutes earlier. Red pixels denote hot spots. Blue pixels denote positions of minima in deuterated methane (CH_3D) equivalent width and thus candidates for opaque clouds. Green regions denote maxima in CH_3D equivalent width and thus regions without opaque clouds. Radiative transfer models were used to calculate synthetic spectra for the zone marked A and the SEB hot spot labeled B.

2. OBSERVATIONS

Five-micron spectra of Jupiter were acquired using NIR-SPEC on the Keck II telescope on 2014 March 11. NIRSPEC is an echelle spectrograph with 3 orders dispersed onto a 1024×1024 InSb array at $5\,\mu m$ at our selected grating/cross-disperser settings of 60.48/36.9 (McLean et al. 1998). A $0.''4 \times 24''$ slit was aligned north–south on the central meridian of Jupiter, resulting in spectra with a resolving power of 20,000. NIRSPEC has an advantage over instrumentation on other telescopes (for example CSHELL on the IRTF) due to the fact that 3 echelle orders at $5\,\mu m$ are placed on the detector array. Thus, each pixel along the slit corresponding to different latitudes on Jupiter has simultaneous spectra at 4.6, 5.0, and $5.3\,\mu m$. In this paper we will focus on Order 16 covering $2131-2165\,\mathrm{cm}^{-1}$ ($4.62-4.69\,\mu m$) and Order 15 which covers $1999-2031\,\mathrm{cm}^{-1}$ ($4.92-5.00\,\mu m$). Jupiter subtended $41''$ and the geocentric Doppler shift was $26.3\,\mathrm{km\,s}^{-1}$. The water vapor column above Mauna Kea was 2 precipitable mm derived from fitting telluric lines in the Jupiter spectra. We did not use stellar spectra for flux calibration or atmospheric transmission because the humidity doubled between the time of the Jupiter and stellar observations. The flux calibration is described in Section 3. Figure 1 shows an image of Jupiter using the SCAM guide camera on NIRSPEC. Although the spectroscopy was performed at $5\,\mu m$, the guide camera works at shorter wavelengths. A K-prime filter centered at $2.12\,\mu m$ was used to obtain sufficient contrast to separate the bands of variable haze reflectivity overlying Jupiter's belts and zones. Two slit positions were required to obtain pole–pole spectra of Jupiter. In Figure 1 spatial pixels that exhibit maxima in flux at $4.66\,\mu m$ are shown in red, locations that exhibit narrow line profiles at
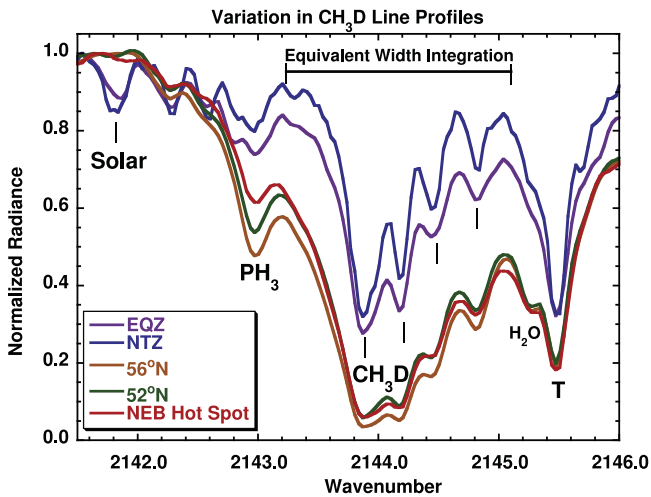
Figure 2. Jupiter spectra at 4.66 μm (NIRSPEC order 16) show dramatic variation with latitude in the strength and width of CH$_3$D lines. Four absorption features are denoted by vertical lines. Narrow CH$_3$D lines are observed in the Equatorial and North Tropical Zones (EQZ, NTZ), but they are much broader in hot spots and at high northern latitudes. A phosphine (PH$_3$) line and a Doppler-shifted H$_2$O line are shown. Fraunhofer lines (CO in the Sun) are only observed in low-flux zones. T denotes telluric lines.

4.66 μm are shown in blue, and regions that have broad pressure-broadened line profiles are shown in green. We focus on two spatial locations with characteristically different spectra: Region A in the South Tropical Zone (STZ) at 32°S, and Region B, a hot spot in the SEB at 17°S. We developed radiative transfer models to calculate synthetic spectra for regions A and B, as described below.

The bandpass at 4.66 μm contains absorption lines of deuterated methane (CH$_3$D), phosphine (PH$_3$), and H$_2$O. Methane and its isotopologues do not condense, and they are not destroyed photochemically, in Jupiter's troposphere. We therefore assume that CH$_4$ and CH$_3$D have a constant mixing ratio with respect to H$_2$ in Jupiter's troposphere, which means that variations in the strength and shape of CH$_4$ and CH$_3$D lines between belts and zones on Jupiter should be due to changes in cloud structure, not gas concentration. Bjoraker et al. (2002) measured the spatial variation of the weak ν_3–ν_4 band of CH$_4$ at 5.18 μm in an attempt to derive cloud structure. Unfortunately, they were unable to calculate synthetic spectra that fit this feature. This is possibly due to inaccurate or incomplete spectroscopic parameters such as line strengths and broadening parameters. Spectroscopic parameters for the much stronger ν_2 fundamental band of CH$_3$D at 2200 cm^{-1}, or 4.5 μm, are well known (Nikitin et al. 1997) and as shown below we now are able to derive cloud structure and spatial variations therein.

Figure 2 shows spectra at 4.66 μm (2144 cm^{-1}, NIRSPEC order 16) of 5 regions in Jupiter's northern hemisphere that exhibit either a maximum in flux (an NEB hot spot at 8.5°N), minima in the equivalent width of CH$_3$D (the EQZ at 0.5°N and NTZ at 23°N), or local maxima in CH$_3$D equivalent width. A horizontal bar indicates the limits that we chose for numerical integration of the equivalent width that includes six absorption lines of CH$_3$D (blended into four at this spectral resolution). All spectra are normalized to 1.0 at 2141.6 cm^{-1} to facilitate comparison of line shapes, since the radiance of the NEB hot spot is 70 times that of the NTZ. A telluric H$_2$O line, its Doppler-shifted counterpart, a PH$_3$ feature, and a Fraunhofer line due to CO in the Sun are also shown. Note that the

Fraunhofer line is observed only in low-flux zone regions such as the EQZ and NTZ. In Sections 3 and 4 we describe how the strength of this feature can be used to constrain cloud models. The equivalent width of the set of CH$_3$D lines at 2144 cm^{-1} varies dramatically from belt to zone. Hot spots and belts exhibit broad pressure-broadened line profiles, while zones have much narrower features that are resolved as 4 distinct CH$_3$D absorption lines. Note that an isolated CH$_3$D line would be spectrally resolved at a resolving power of 20,000 (0.11 cm^{-1} resolution). This is because molecules such as CH$_3$D typically have broadening coefficients of 0.06 cm^{-1}/atm and the line formation region on Jupiter at 4.66 μm takes place at pressures greater than 2 bars.

3. DATA ANALYSIS AND RESULTS

Absolute flux calibration was performed for both NIRSPEC orders 15 and 16 by smoothing the spectrum of the NEB hot spot at 8.5°N to 4.3 cm^{-1} resolution, dividing by the transmittance of the Earth's atmosphere above Mauna Kea, and scaling the radiance of the resulting spectrum to an average of the 4 hottest spectra of Jupiter's NEB observed by *Voyager IRIS* in 1979.

In addition to pressure-broadened line profiles, the spectrum at 4.66 μm provides valuable information on the ratio of reflected sunlight to thermal emission on Jupiter, which is critical for understanding Jupiter's cloud structure. We compared the equivalent width of the Fraunhofer line at 2141.8 cm^{-1} with its measured value in the Sun using data from the Atmospheric Trace Molecule Spectroscopy (ATMOS) experiment which flew on the space shuttle Challenger in 1985 (Farmer & Norton 1989; Farmer et al. 1994). Solar Fraunhofer lines in spectra of Jupiter arise from regions with a significant fraction of reflected sunlight, such as locations with thick high clouds. Fraunhofer lines are not observed in regions that are dominated by thermal emission, such as hot spots. We selected a zone at 32°S (marked "A" on Figures 1, 4, and 5) for further study based on the strength of this particular Fraunhofer line. It is 43% as strong as in the Sun; thus, 57% of the flux consists of thermal emission originating in the deep atmosphere that has been attenuated by one or more cloud layers before escaping to space. This thermal flux preserves the broad line profiles of CH$_3$D caused by collisions with H$_2$ and He in its line formation region at the deepest levels probed. We excluded the spectrum of the NTZ shown in Figure 2 for studies of the deep atmosphere because the Fraunhofer line is 95% as strong as in the Sun; thus, there is insufficient thermal flux to constrain the deep cloud structure at 23°N. We also modeled the SEB hot spot at 17°S and 208°W (marked "B" on Figures 1, 4, and 5), which had the highest radiance in our entire dataset. The noise level was measured using the standard deviation of the number of counts in the spectral pixel corresponding to a saturated telluric water line in each order. This was evaluated over 11 spatial pixels over the lowest flux region (the STZ) and also for 11 spatial pixels off of Jupiter. Both gave the same result. In Order 16 the signal to noise ratio (S/N) of the SEB hot spot at 2141.6 cm^{-1} was 2500; the S/N of the zone at 32°S was 48. In Order 15 where strong H$_2$O lines occur, the S/N of the same hot spot was 1900 at 2012.2 cm^{-1}; the S/N of the STZ was 35. Synthetic spectra were calculated using the Spectrum Synthesis Program radiative transfer code as described in Kunde & Maguire (1974). The input temperature profile was obtained from the Galileo Probe (Seiff et al. 1998). Line
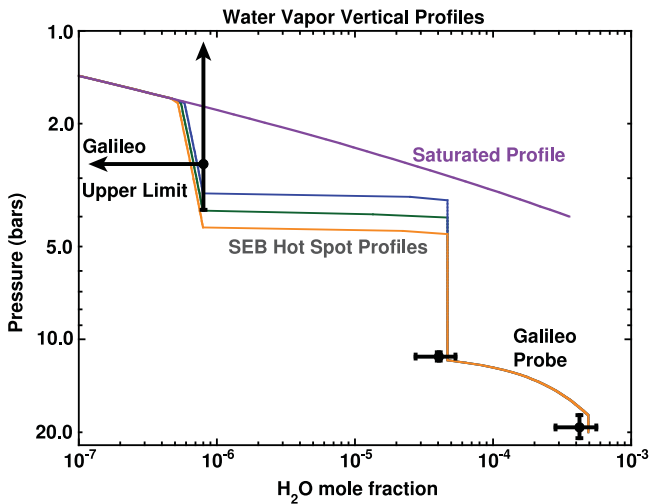
Figure 3. Vertical profiles of H_2O used to calculate synthetic spectra in Figures 4 and 5.

parameters for CH_3D and other $5 \mu m$ absorbers are from GEISA 2003 (Jacquinet-Husson et al. 2005). Parameters for CH_3D-H_2 and CH_3D-He broadening have been measured in the lab (Boussin et al. 1999; Féjard et al. 2003; Lerot et al. 2003). We used a broadening coefficient of $0.0613 \, cm^{-1}/atm$ $(296/T)^{0.5}$ for CH_3D colliding with a mixture of 86.3% H_2 and 13.6% helium, as measured by the Galileo Probe (von Zahn et al. 1998). Pressure-induced H_2 coefficients were obtained using laboratory measurements at $5 \mu m$ by Bachet et al. (1983) and the formalism developed by Birnbaum & Cohen (1976).

The base of the model was set to 20 bars, 416 K for the SEB hot spot to ensure that the base was well below the level where Jupiter's atmosphere becomes optically thick due to pressure-induced H_2 opacity. For the zone at 32°S, we investigated lower boundaries at 2, 4, 5, and 20 bars to simulate opaque NH_4SH clouds, H_2O clouds, and no deep clouds in the troposphere. For the hot spot, we calculated a spectrum free of deep clouds for an emission angle of $18°.7$ and for an H_2O mole fraction of 47 ppm for $P > 4.5$ bars as shown in Figure 3, consistent with results from the Galileo Probe (Wong et al. 2004b). The model was iterated to fit CH_3D (0.18 ppm) and PH_3 (0.45 ppm). Our fit to CH_3D in the hot spot is very close to the value (0.16 ± 0.04 ppm) derived by Lellouch et al. (2001) using spectra at $8.6 \mu m$ from the *Infrared Space Observatory*. We then convolved the Jupiter spectrum to 0.02 cm^{-1}, Doppler-shifted it by $25.2 \, km \, s^{-1}$, multiplied by the calculated transmittance above Mauna Kea, convolved it to $0.14 \, cm^{-1}$ to match the NIRSPEC data, and multiplied the spectrum by 0.332 to simulate the transmission of upper cloud layers on Jupiter to match the observed continuum. As shown in Figure 4, the synthetic spectrum fits Region B, the SEB hot spot spectrum without any deep cloud opacity ($P > 2$ bars). All 4 CH_3D features, including the wing between 2143.2 and 2143.6 cm^{-1} are matched.

The zone model is more complicated. A radiative transfer model was used to calculate spectra for an emission angle of $33°.4$. Above each lower boundary, the gas composition was set to 0.18 ppm CH_3D. For the zone model with no deep clouds, the Galileo Probe H_2O profile was used. For models with opaque clouds at 2, 4, and 5 bars, a saturated profile of H_2O was used (see Figure 3). The mole fraction of PH_3 was iterated

to a value of 0.7 ppm to match the absorption feature at $2143 \, cm^{-1}$ for lower boundaries at 4 and 5 bars. For the zone model without deep clouds, the PH_3 abundance in the STZ was iterated to a value of 0.45 ppm. Thus, PH_3 can also be used to discriminate between deep cloud models, as we describe below. A larger PH_3 mole fraction (0.7 ppm) above an opaque cloud layer at 4 bars yields the same PH_3 absorption as a smaller mole fraction (0.45 ppm) above the (deeper) level where the atmosphere becomes opaque due to H_2–H_2 opacity. The synthetic spectrum was split into two parts. The reflected solar component was calculated using the transmittances above a reflecting layer at 300 mbar and for an upper cloud reflectance of 9%. It was convolved to 0.02 cm^{-1} resolution, Doppler-shifted, and multiplied by the ATMOS solar spectrum. The thermal component was convolved, Doppler-shifted, and multiplied by transmittances of 0.393, 0.0269, 0.016, and 0.0038 for models with a base of 2, 4, 5, and 20 bars, respectively, and added to the reflected spectrum. This, in turn, was multiplied by the transmission above Mauna Kea and finally convolved to 0.14 cm^{-1} resolution.

Due to the numerous parameters in this model, we illustrate the parameter sensitivity of the model for the reflected solar and thermal components of the zone model separately in Figure 5. We treat the reflective upper cloud as spectrally gray. Ice components such as NH_3, NH_4SH, and H_2O have been seen at other wavelengths (e.g., Brooke et al. 1998; Simon-Miller et al. 2000; Baines et al. 2002; Wong et al. 2004a; Sromovsky & Fry 2010). However, our spectral windows do not include significant ice absorption features. The imaginary indices of refraction of NH_3 (Martonchik et al. 1984) and NH_4SH (Howett et al. 2007) are on the order of 10^{-3} at the wavelengths studied here, much lower than values closer to unity at the ν_3 vibration transitions for these ices (at 3.0 and 3.4 μm, respectively). Thus, the spectral features in the reflected solar component are due to CH_3D absorption lines in the upper troposphere of Jupiter or Fraunhofer lines in the Sun.

In the top panel of Figure 5 we show 4 Fraunhofer lines, marked S. The strength of the strongest Jovian feature at $2141.8 \, cm^{-1}$ when compared with the spectrum of the Sun acquired by the ATMOS investigation yields the relative fractions of reflected sunlight (0.43) and thermal emission (0.57) for this portion of Jupiter's STZ. The fraction of reflected sunlight combined with the calibrated continuum level allows us to derive an upper cloud reflectance of 9%. There are 5 CH_3D absorption features in this spectral range. Ammonia clouds and hazes limit the penetration of reflected sunlight to the upper troposphere. We investigated the pressure of the reflecting layer by calculating spectra at 100, 300, and 600 mbars. We adopted a value of 300 mbars for the STZ. Note that in order to match the narrow absorption cores of CH_3D in a model that consists of the sum of two components, there are a family of solutions for the pressure level of the solar reflecting layer and for the thermal cloud top pressure. Increasing the pressure of the reflecting layer from 300 to 600 mbars may be compensated by, for example, decreasing the (deep) cloud top pressure from 4 to 2 bars in the thermal component. However, we can exclude this possibility by studying the wing of the CH_3D feature between 2143.2 and 2143.6 cm^{-1}. The top panel shows that the reflected solar spectrum is flat over this range. In contrast, each thermal model has a different CH_3D wing line slope. We now return to Figure 4 which compares the
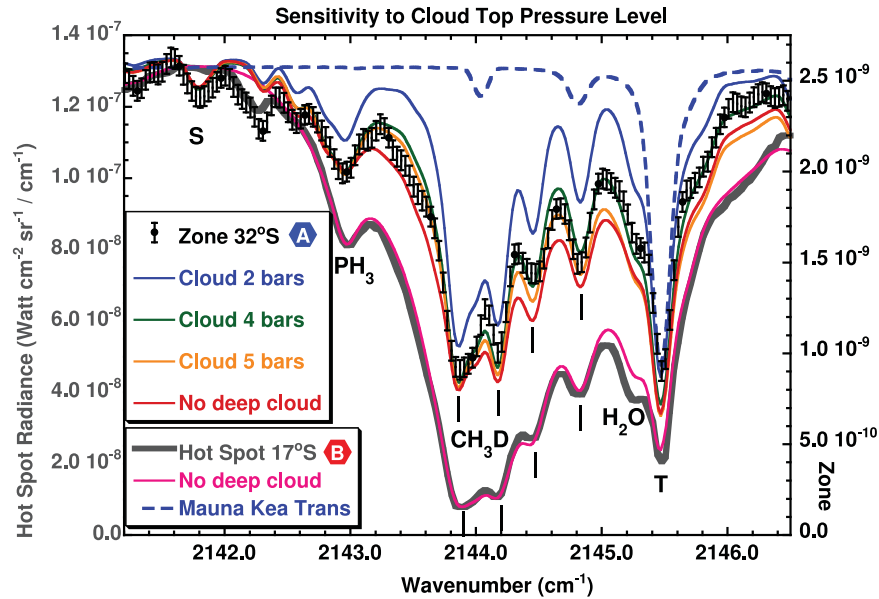
Figure 4. The pressure level of deep clouds on Jupiter as constrained by CH$_3$D line profiles observed in Order 16. An SEB hot spot (gray curve) at 17°S (labeled B in Figure 1) is fitted without any clouds at pressures greater than 2 bars (pink curve). Hot spot error bars would be smaller than the thickness of the gray curve. The spectrum of the STZ at 32°S (points with error bars, and labeled A in Figure 1) was modeled using opaque clouds at 2, 4, 5 bars and a model without any deep clouds. We may exclude an opaque NH$_4$SH cloud at 2 bars due to the poor fit of the blue curve to the observed spectrum. The best fit requires an opaque cloud between 4 and 5 bars. Thermochemical models predict that cloud opacity at this pressure level is due to a water cloud. Note the factor of 50 difference in radiance scales between the hot spot and the zone spectra. The calculated transmittance above Mauna Kea for 2 mm precip H$_2$O is shown as a dashed blue line. T denotes a telluric H$_2$O line and S denotes a solar (Fraunhofer) line.

sum of the reflected and thermal components of each model to the observed STZ spectrum. We can exclude models with an opaque NH$_4$SH cloud at 2 bars (blue curve) as well as the model with no deep cloud (red curve). Note that the calculated radiances for both of these models lie well outside the error bars of the zone spectrum. The model with a deep cloud at 5 bars fits portions of the spectrum but the model with an opaque cloud at 4 bars (green curve) provides a better overall fit to the spectrum.

The NIRSPEC spectral bandpass for Order 16 covers more than just this particular CH$_3$D absorption feature. In Figure 6 we compare the STZ spectrum with the same zone models for a spectral region adjacent to the one displayed in Figures 4 and 5. Here there are three telluric H$_2$O lines. To the left of each telluric line is a Jovian water line redshifted by 0.18 cm^{-1} due to the relative velocity of Jupiter with respect to the Earth. The wings of these water lines permit us to discriminate between models. The best fit requires an opaque cloud between 4 and 5 bars.

Next, we compare our retrieved PH$_3$ abundances in the 4 to 8-bar level of the STZ with measurements of PH$_3$ at 1 bar from the Cassini flyby of Jupiter in 2001 January . Irwin et al. (2004) retrieved PH$_3$ mole fractions on Jupiter ranging from 0.9 to 1.5 ppm using zonal averages of CIRS spectra at 9 μm between 60°S and 60°N. The retrieved PH$_3$ mole fraction at 32°S was 1.0 $\pm$ 0.2 ppm. Phosphine falls off with height in the upper troposphere due to ultraviolet photolysis, but its mole fraction is not expected to change between 1 and 8 bars. There remain discrepancies between PH$_3$ retrievals at 5 and 9 μm (Fletcher et al. 2009). Nevertheless, better agreement for the abundance of PH$_3$ at 32°S is achieved for a model with opaque clouds near 4–5 bars (0.7 ppm) than for a zone model with no deep cloud (0.45 ppm).

Thus, using three independent arguments that are based on: (a) the slope of the CH$_3$D line wings, (b) the slope of the H$_2$O line wings, and (c) the derived mole fractions of PH$_3$, we conclude that there must be significant cloud opacity between 4 and 5 bars in the STZ at 32°S. Based on the temperatures at these pressure levels (257–275 K), thermochemical models predict that this is a water cloud.

In Figure 7 we compare the spectrum of the SEB hot spot marked B at 2016 cm^{-1} (4.96 μm) with 3 different models calculated using the vertical profiles of H$_2$O shown in Figure 3. The parameters are the same as those used to fit the spectrum at 2144 cm^{-1} except for H$_2$O and NH$_3$. We initially used a vertical profile of NH$_3$ derived from absorption of the radio signal from the Galileo Probe (Folkner et al. 1998 as modified by Hanley et al. 2009). We found that a scaling factor of 2 was required to fit the NH$_3$ absorption features shown in Figure 7. This corresponds to NH$_3$ mole fractions ranging from 240 ppm at 2 bars to 600 ppm at 4.5 bars. This is significantly larger than values derived from ground-based microwave observations (see Sault et al. 2004). However, we have not used the much stronger absorption features in Order 14 (5.3 μm) to constrain the NH$_3$ vertical profile. Thus, the NH$_3$ mole fractions reported here should be regarded as preliminary. The three different vertical profiles of H$_2$O in Figure 3, and used in our calculations, were based on the mass spectrometer data on the Galileo Probe. Niemann et al. (1998) reported an upper limit to H$_2$O of 0.8 ppm at 2.7 bars. Wong et al. (2004b) reported a mole fraction of H$_2$O of 40 $\pm$ 13 ppm at 11.0–11.7 bars on Jupiter. The only adjustable parameter in our model was the pressure at which the H$_2$O mole fraction increased from 0.8 to 47 ppm, as shown in Figure 3. The best fit is for a pressure of 4.5 bars. Assuming that the SEB hot spot is similar to the one that Galileo entered, this data point provides a useful measurement of the depth at which dynamical
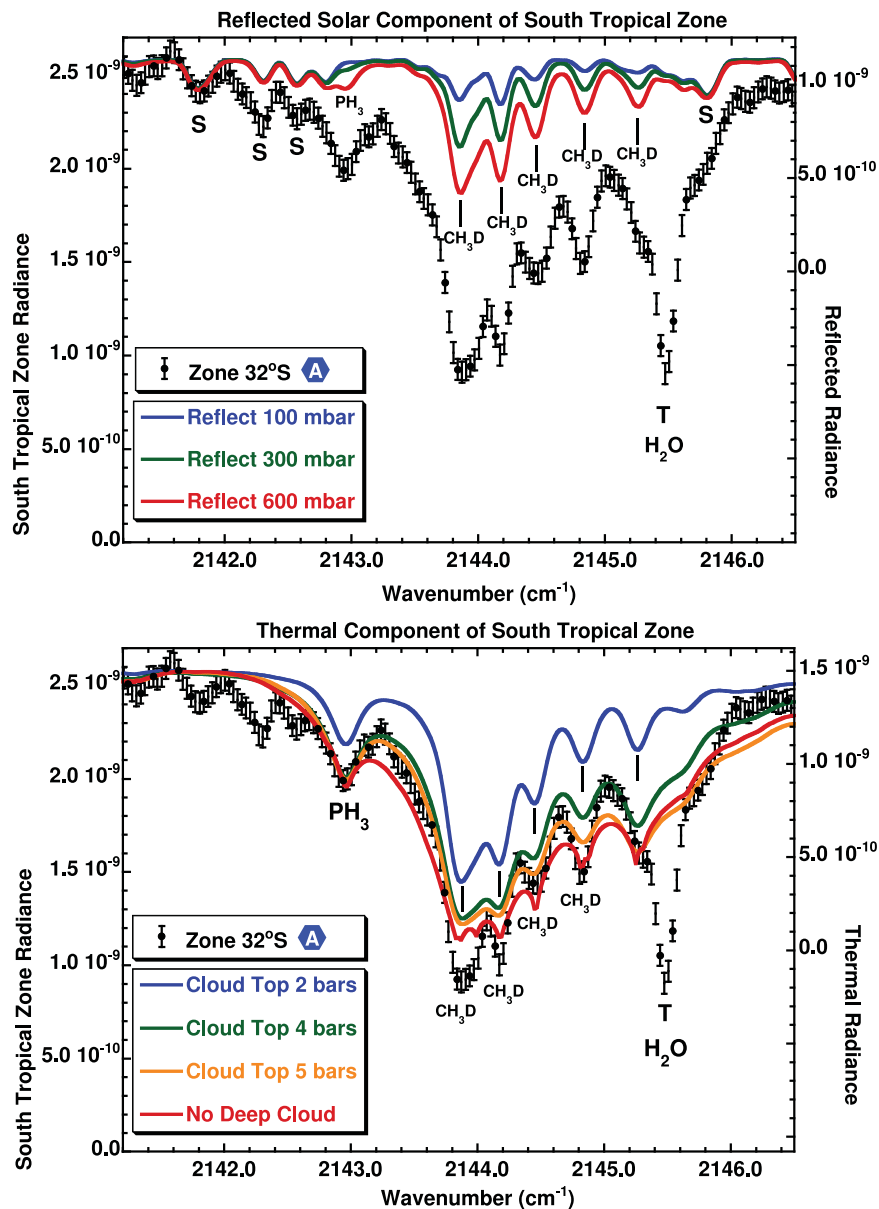
Figure 5. Top: the reflected solar component of a radiative transfer model of the STZ at 32°S. Four Fraunhofer lines are marked as S. A telluric H_2O line is marked as T. A reflecting layer is placed at 100, 300, and 600 mbars in Jupiter's upper troposphere. One PH_3 and five CH_3D lines are shown. The narrow cores of the CH_3D lines are sensitive to the solar component. Bottom: the thermal component is shown for models with cloud tops at 2, 4, and 5 bars, and for a model with no deep cloud. The wing of CH_3D between 2143.2 and 2143.6 cm^{-1} and the PH_3 line at 2143.0 cm^{-1} are due to the thermal component. Radiance scales are offset to match the continuum of the observed spectrum.

processes have dried out hot spots on Jupiter. This depth compares well with the depth determined by Sault et al. (2004) for the NH_3 abundance in hot spots from microwave observations.

We next modeled the zone marked A at 2016 cm^{-1}. We used the same procedure as was used to model the zone spectrum at 2144 cm^{-1}. We explored the same set of models with cloud tops at 2, 4, and 5 bars, as well as the model with no deep cloud. This portion of Jupiter's spectrum is not sensitive to the deep cloud structure. Using the results from fitting CH_3D, we adopted a model with an opaque cloud top at 4.0 bars and a saturated H_2O profile above. The NH_3 mole fraction was iterated until a rough fit was achieved using a value of 250 ppm between 0.75 and 4.0 bars and a saturated value for $P < 0.75$ bars. Without any obvious Fraunhofer lines in this spectral

region to constrain the reflected solar component, we assumed the same upper cloud reflectance of 9% as at 2144 cm^{-1} and we obtained an upper cloud transmittance of 0.0542. The transmittance is therefore less certain than the value derived at 2144 cm^{-1}. The principal conclusion from this spectral region is that the observed H_2O line profiles in the STZ are slightly broader than the telluric H_2O features, but narrower than H_2O features in the SEB hot spot. A saturated H_2O profile for $P < 4.0$ bars provides a satisfactory fit to the observed spectrum.

4. DISCUSSION

This paper describes a technique to determine water cloud heights using spectrally resolved line shapes of CH_3D. We have demonstrated with a set of spectra from characteristic
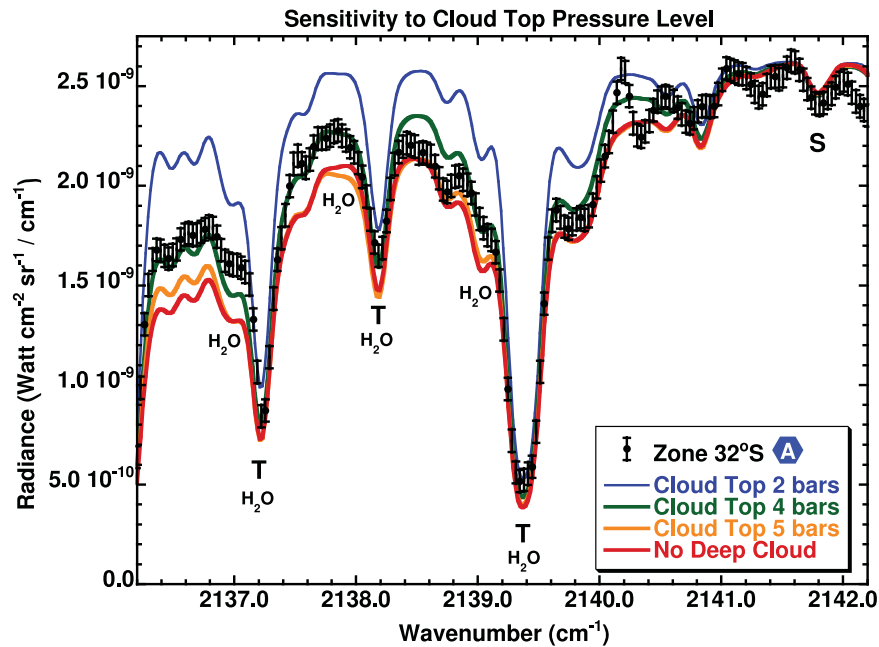
Figure 6. The spectrum of the STZ at 32°S and radiative transfer models with opaque clouds at 2, 4, and 5 bars, and a model without any deep clouds are shown for a spectral region adjacent to the CH_3D features. T denotes telluric H_2O lines and S denotes a solar (Fraunhofer) line. Note the 3 Jovian H_2O lines redshifted by $0.18 \ cm^{-1}$ from their telluric counterparts. The wings of these water lines permit us to discriminate between models. The best fit requires an opaque cloud between 4 and 5 bars.
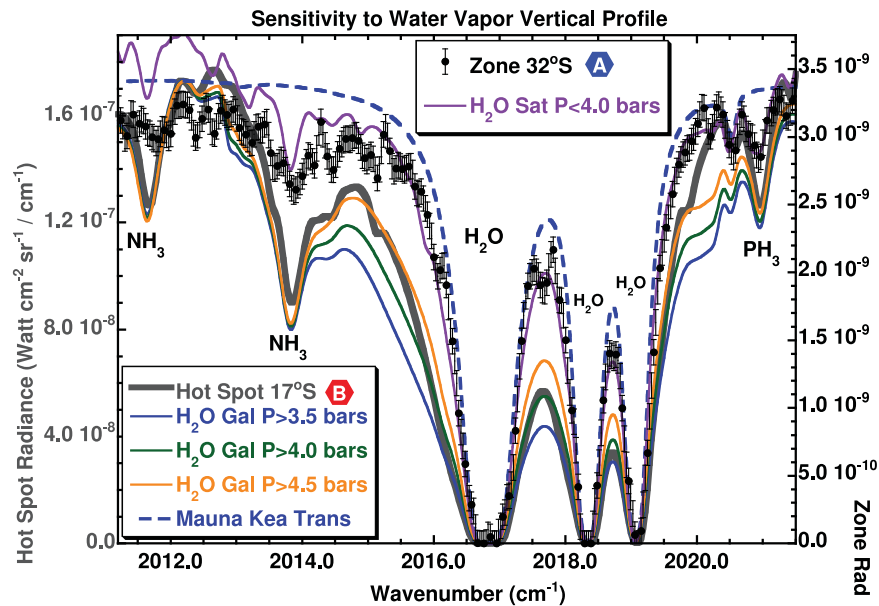
Figure 7. Vertical profiles of water vapor mixing ratio as constrained by H_2O line profiles observed in Order 15. An SEB hot spot (Region B, gray curve) at 17°S is fitted without any deep clouds. Hot spot error bars would be smaller than the thickness of the gray curve. Three vertical profiles of H_2O were calculated for the hot spot. The best fit used the Galileo Probe value for H_2O for pressures greater than 4.5 bars (see also Figure 3). The spectrum of the STZ at 32°S (Region A, points with error bars) was fitted using an opaque cloud at 4 bars and a saturated H_2O profile above it (purple curve). The H_2O lines in the zone are slightly broader than the telluric features, but much narrower than in the hot spot.

spatial regions that variation in the water cloud height manifests as a variation in the equivalent width of CH_3D. This technique can be applied to all regions covered by the spectrometer slit. We show the CH_3D equivalent width as a function of latitude (black curve) in Figure 8, highlighting the latitude regions which may have water clouds. The observations are extremely valuable both for understanding Jupiter's atmospheric circulation, as well as its bulk water abundance (a constraint on planetary formation scenarios).

However, the equivalent width of CH_3D alone is not sufficient. In order to map H_2O clouds on Jupiter, we need to measure the latitudinal profile of both CH_3D line shapes as well as the strength of the Fraunhofer line at $2141.8 \ cm^{-1}$. In Figure 8 we plot three quantities as a function of latitude on Jupiter. First is the radiance integrated over the $4.6 \ \mu m$ bandpass and normalized to 1.0 as a function of spatial pixel and converted to planetographic latitude. This is shown in red. The next quantity is the equivalent width of our set of
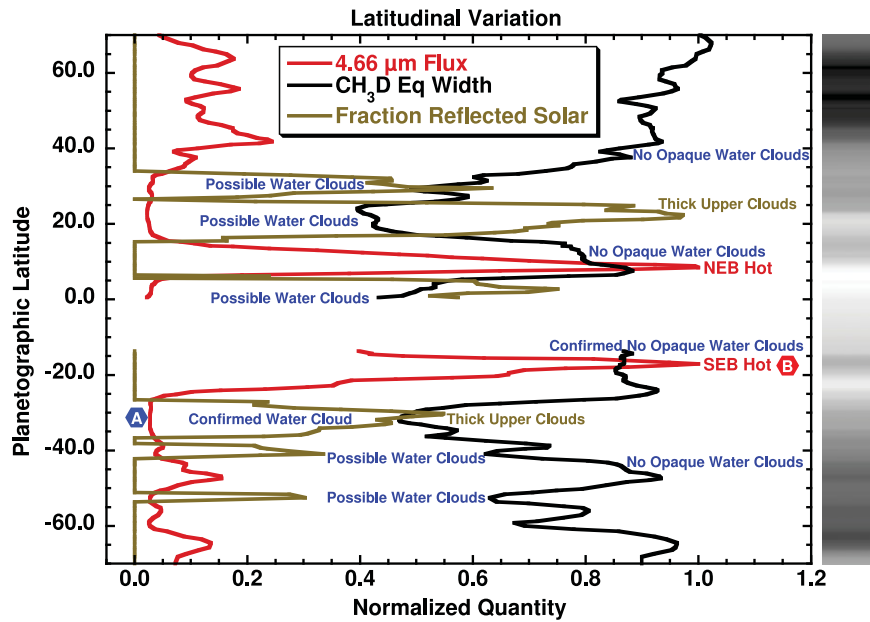
Figure 8. Flux at 4.66 μm (red curve), the equivalent width of CH$_3$D (black curve), and the the ratio of the equivalent width of the Fraunhofer line at 2141.8 cm^{-1} on Jupiter to that in the Sun is shown for each latitude along the central meridian on Jupiter. Hot spots are present at 8.5°N and 17°S. Latitudes exhibiting minima in CH$_3$D equivalent widths are candidates for water clouds. Radiative transfer models were used to match a zone spectrum at 32°S (marked "A") and a hot spot spectrum at 17°S (marked "B"). The gold curve indicates the fraction due to reflected sunlight. Large values imply thick upper clouds that attenuate thermal radiation from below and reflect sunlight above. The bar on the right denotes haze reflectivity variation with latitude obtained from 2.12 μm SCAM images, roughly similar to belt-zone structure seen at visible wavelengths.

CH$_3$D absorption lines integrated between 2143.21 and 2145.04 cm^{-1} (denoted by the horizontal bar in Figure 2). This is shown in black. The last quantity plotted in Figure 8 is the fraction of reflected sunlight as a function of latitude. This was obtained by measuring the equivalent width of the Fraunhofer line at 2141.8 cm^{-1} as a function of latitude and dividing it by the value in the Sun as measured by ATMOS. At latitudes such as 23°N where this value is close to 1.0, there is insufficient thermal flux to constrain the deep cloud structure. However, by using adjacent latitudes where CH$_3$D equivalent widths are also small, and where the fraction of reflected solar flux <0.6, we can infer the presence of water clouds. Thus, we have indicated "possible water clouds" for the entire region where values of CH$_3$D equivalent width are small. The vertical bar on the right denotes the brightness of Jupiter in reflected sunlight at 2.12 μm obtained from SCAM images navigated onto a planetographic latitude grid. This wavelength sounds hazes in the upper troposphere and illustrates Jupiter's belt-zone structure.

The equivalent width of CH$_3$D is sensitive to two parameters: the fraction of reflected sunlight and the pressure level of the deep cloud. Consider two regions on Jupiter. They both lack an opaque water cloud, but one has thin upper clouds so that the 5 μm spectrum is 100% thermal. The other has a thick, reflective upper cloud that attenuates the thermal component yielding a spectrum that is 50% thermal and 50% reflected solar. In the latter case, the contribution of the reflected solar continuum will significantly reduce the equivalent width of the CH$_3$D absorption features that are present in the thermal component. A low value of CH$_3$D equivalent width might be interpreted as due to a deep water cloud, whereas in this case the small equivalent width was due solely to the presence of the solar component from an upper reflective layer. Thus, we have to be cautious in using the equivalent width of

CH$_3$D alone to infer deep cloud structure. Nevertheless, the data plotted in Figure 8 show interesting structure at latitudes where the fraction of reflected solar radiation is essentially zero. High latitudes, southward of 55°S and northward of 35°N show interesting variations in CH$_3$D equivalent widths that cannot be attributed to reflected sunlight and thus are related to deep cloud structure.

With the caveat that radiative transfer modeling is required to verify the presence of water clouds in regions with small CH$_3$D equivalent widths and significant fractions of reflected sunlight, we can make the following conclusions: Where thick water clouds are present at pressures in the 3–5 bar range, the CH$_3$D equivalent width is small, and the black curve (Figure 8) tends toward lower values. Regions with thick, high-altitude ($P \leqslant 4$ bars) water clouds can be associated with widespread upwelling, since downwelling would provide the opposite effect of clearing cloud opacity via sublimation. We find the smallest CH$_3$D equivalent widths in the three low-latitude zones: the EQZ and the north and south tropical zones. This implies a large vertical extent to the upwelling responsible for forming the thick white clouds observed in zones at optical wavelengths.

Thick water clouds in zones specifically contradict models of inverted two-layer circulation within the tropospheric cloud decks. Ingersoll et al. (2000) and Showman & de Pater (2005) suggested inverted two-layer circulation schemes to explain widespread ammonia gas depletion even in zones. In this type of circulation model, regions of upwelling (thick clouds) in the visible upper levels (NH$_3$+ NH$_4$SH cloud decks) corresponds to downwelling at the deeper, hidden water cloud level. Our results suggest that mass flux into the upper cloud layers of zones is not dominated by horizontal transport, as in the Showman & de Pater scenario, but is driven by vertical transport from below. Jupiter's circulation in zones therefore

maintains the same sign of upwelling/downwelling across the full 0.5–5 bar weather layer. The same sign of upwelling/downwelling over this large an extent was also derived by de Pater et al. (2010) from 5 μm bright rings around vortices. These authors suggested that vortices must extend vertically from at least the 4–7 bar level up to the tropopause.

Large CH$_3$D equivalent width requires low water cloud opacity. Subsidence of dry upper-level air provides the simplest mechanism. Figure 8 shows that at low latitudes, the clearest deep atmosphere (high values of the black curve) occur where the 5 μm flux is highest (red curve). The very highest flux levels correspond to an atmosphere largely devoid of clouds of all three types, H$_2$O, NH$_3$, and NH$_4$SH, again suggesting downwelling circulation that spans the full 0.5–5 bar range at least. However, the width (in latitude) of the 5 μm flux peak is very narrow, compared to the width of the NEB/SEB regions with low water cloud opacity. Thus, over a broad latitude range with little or no water cloud opacity, the atmosphere is characterized by both cloudy and cloud-free conditions at the upper levels. Perhaps a two-layer circulation model with a vertical flow reversal layer between the water and NH$_3$/NH$_4$SH clouds can be relevant on these regional scales, if not for the entire planet.

The rapid "fading" or whitening of the South Equatorial Belt between 2008 and 2010 was interpreted by Fletcher et al. (2011) as due to enhanced upwelling of ammonia-rich air followed by condensation. Using CH$_3$D line profiles and absorption lines of NH$_3$ and H$_2$O in the 5 μm window, we now have the capability of measuring cloud structure and volatile abundances in the NEB and SEB at the 4–8 bar level. Any future changes in the appearance of the belts can now be investigated over the full 0.5–8-bar range of Jupiter's troposphere using spectroscopy at 4.6 and 8.6 μm. By studying changes in each cloud layer separately we will have a much better understanding of the dynamics below Jupiter's visible clouds.

The high latitudes also show high CH$_3$D equivalent widths. Here, more detailed modeling will be needed to disentangle geometric effects caused by viewing geometry, as well as changes in atmospheric scale height in a rapidly rotating nonspherical planet. But the data do suggest a different paradigm in deep cloud structure at high latitudes (polewards of 40°). We note, though, that 5 μm images at high spatial resolution show a lot of structure at these latitudes (de Pater et al. 2011), and microwave images show an overall low NH$_3$ abundance (de Pater 1986). A combination of 5 μm imaging, microwave imaging, and 5 μm spectroscopy of Jupiter's polar regions would be extremely useful to investigate these interesting cloud features.

We now return to the interpretation of 5 μm spectra of Jupiter acquired by the KAO, *Voyager*/*IRIS*, and Galileo/NIMS. It now seems clear that the airborne observations of Jupiter were flux-weighted by hot spots. The abundances of H$_2$O and other molecules derived by Bjoraker et al. (1986a, 1986b) pertain to hot spots, but not to Jupiter as a whole. The lower boundary for hot spots is in fact due to pressure-induced H$_2$ opacity, rather than an opaque water cloud, as proposed by Carlson et al. (1992). However, the model proposed by Carlson et al. does appear to apply to Jupiter's zones, at least in the regions marked in Figure 8 as candidates for water clouds. Similarly, models of Galileo/NIMS spectra of the EQZ by Drossart et al. (1998) are probably

accurate while models of hot spots that included water clouds (e.g., Nixon et al. 2001) will need to be revised.

This technique provides a constraint on Jupiter's deep water abundance and therefore its O/H ratio. The base of the water cloud is sensitive to the abundance of water because higher abundances lead to condensation at deeper levels. The data provide the level of the cloud top, not the cloud base. Since the top is at higher altitude than the base, cloud top constraints provide lower limits to the pressure of the cloud base, or, lower limits to the deep abundance of water. A spectrum requiring a water cloud at $P \geqslant 5$ bar would establish a supersolar enrichment of water in Jupiter, better constraining planetary formation models (Wong et al. 2008).

Figure 4 shows the effect of water cloud pressure level on model fits to a cloudy zone spectrum at 32°S. The spectrum is best fit by a water cloud with a top between 4 and 5 bars. The cloud base is therefore found at $P > 4 - 5$ bar. Following Figure 1 in Wong et al. (2008), a cloud base at 4–5 bar corresponds to O/H ratios 0.33–1.1×solar (corrected to the new solar O/H ratio of Asplund et al. 2009). Our observations thus provide a lower limit to Jupiter's water abundance of 0.33–1.1× solar. This result is consistent with the Galileo Probe lower limit of 0.48 ± 0.16× solar (Wong et al. 2004b), and therefore does not provide any new constraint on the water abundance. In future work, we will search for spectra that require an even deeper water cloud.

Knowledge of the deep cloud structure permits us to retrieve abundances of H$_2$O, NH$_3$, and other 5 μm absorbers more accurately. This will enable studies of dynamics below Jupiter's visible cloud layers. Additional observations will permit us to observe discrete cloud features such as the Great Red Spot and Oval BA.

Facilities: Keck:II, *Voyager* (*IRIS*).

REFERENCES

Adriani, A., Filacchione, G., Di Iorio, T., et al. 2014, SSRv
Asplund, M., Grevesse, N., Sauval, A. J., & Scott, P. 2009, ARA&A, 47, 481
Bachet, G., Cohen, E. R., Dore, P., & Birnbaum, G. 1983, CaJPh, 61, 591
Baines, K. H., Carlson, R. W., & Kamp, L. W. 2002, Icar, 159, 74
Birnbaum, G., & Cohen, E. R. 1976, CaJPh, 54, 593
Bjoraker, G. L., Hewagama, T., & Orton, G. S. 2002, BAAS, 34, 874
Bjoraker, G. L., Larson, H. P., & Kunde, V. G. 1986a, ApJ, 311, 1058
Bjoraker, G. L., Larson, H. P., & Kunde, V. G. 1986b, Icar, 66, 579
Boussin, C., Lutz, B. L., Hamdounia, A., & de Bergh, C. 1999, JQSRT, 63, 49
Brooke, T. Y., Knacke, R. F., Encrenaz, T., et al. 1998, Icar, 136, 1
Carlson, B. E., Lacis, A. A., & Rossow, W. B. 1992, ApJ, 388, 648
de Pater, I. 1986, Icar, 68, 344

de Pater, I., DeBoer, D., Marley, M., Freedman, R., & Young, R. 2005, Icar, 173, 425

de Pater, I., Wong, M. H., de Kleer, K., et al. 2011, Icar, 213, 559

de Pater, I., Wong, M. H., Marcus, P., et al. 2010, Icar, 210, 742

Drossart, P., Roos-Serote, M., Encrenaz, T., et al. 1998, JGR, 103, 23043

Farmer, C. B. 1994, in IAU Symp. 154, Infrared Solar Physics, ed. D. M. Rabin, J. T. Jefferies, & C. Lindsey, 511

Farmer, C. B., & Norton, R. H. 1989, A High-resolution Atlas of the Infrared Spectrum of the Sun and the Earth Atmosphere from Space, A compilation of ATMOS spectra of the region from 650 to 4800 cm^{-1} (2.3 to 16 μm), Vol. I (Dordrecht: Kluwer)

Féjard, L., Gabard, T., & Champion, J.-P. 2003, JMoSp, 219, 88

Fletcher, L. N., Orton, G. S., Rogers, J. H., et al. 2011, Icar, 213, 564

Fletcher, L. N., Orton, G. S., Teanby, N. A., & Irwin, P. G. J. 2009, Icar, 202, 543

Folkner, W. M., Woo, R., & Nandi, S. 1998, JGR, 103, 22847

Friedson, A. J. 2005, Icar, 177, 1

Hanley, T. R., Steffes, P. G., & Karpowicz, B. M. 2009, Icar, 202, 316

Hersant, F., Gautier, D., & Lunine, J. I. 2004, P&SS, 52, 623

Howett, C. J. A., Carlson, R. W., Irwin, P. G. J., & Calcutt, S. B. 2007, JOSAB, 24, 126

Ingersoll, A. P., Gierasch, P. J., Banfield, D., Vasavada, A. R., & Galileo Imaging Team 2000, Natur, 403, 630

Irwin, P. G. J., Parrish, P., Fouchet, T., et al. 2004, Icar, 172, 37

Jacquinet-Husson, N., Scott, N. A., Chedin, A., et al. 2005, JQSRT, 95, 429

Janssen, M. A., Hofstadter, M. D., Gulkis, S., et al. 2005, Icar, 173, 447

Kunde, V. R., & Maguire, W. C. 1974, JQSRT, 14, 803

Larson, H. P., Fink, U., Treffers, R., & Gautier, T. N., III 1975, ApJL, 197, L137

Lellouch, E., Bézard, B., Fouchet, T., et al. 2001, A&A, 370, 610

Lerot, C., Walrand, J., Blanquet, G., Bouanich, J.-P., & Lepère, M. 2003, JMoSp, 219, 329

Martonchik, J. V., Orton, G. S., & Appleby, J. F. 1984, ApOpt, 23, 541

McLean, I. S., Becklin, E. E., Bendiksen, O., et al. 1998, Proc. SPIE, 3354, 566

Niemann, H. B., Atreya, S. K., Carignan, G. R., et al. 1998, JGR, 103, 22831

Niemann, H. B., Harpold, D. N., Atreya, S. K., et al. 1992, SSRv, 60, 111

Nikitin, A., Champion, J. P., Tyuterev, V. G., & Brown, L. R. 1997, JMoSp, 184, 120

Nixon, C. A., Irwin, P. G. J., Calcutt, S. B., Taylor, F. W., & Carlson, R. W. 2001, Icar, 150, 48

Orton, G., Ortiz, J. L., Baines, K., et al. 1996, Sci, 272, 839

Ragent, B., Colburn, D. S., Rages, K. A., et al. 1998, JGR, 103, 22891

Roos-Serote, M., Atreya, S. K., Wong, M. K., & Drossart, P. 2004, P&SS, 52, 397

Sault, R. J., Engel, C., & de Pater, I. 2004, Icar, 168, 336

Seiff, A., Kirk, D. B., Knight, T. C. D., et al. 1998, JGR, 103, 22857

Showman, A. P., & de Pater, I. 2005, Icar, 174, 192

Simon-Miller, A. A., Conrath, B., Gierasch, P. J., & Beebe, R. F. 2000, Icar, 145, 454

Sromovsky, L. A., & Fry, P. M. 2010, Icar, 210, 230

Weidenschilling, S. J., & Lewis, J. S. 1973, Icar, 20, 465

Wong, M. H., Atreya, S. K., Kuhn, W. R., Romani, P. N., & Mihalka, K. M. 2015, Icar, 245, 273

Wong, M. H., Bjoraker, G. L., Smith, M. D., Flasar, F. M., & Nixon, C. A. 2004a, P&SS, 52, 385

Wong, M. H., Lunine, J., Atreya, S. K., et al. 2008, in Oxygen in the Solar System, Vol. 68, ed. G. J. MacPherson et al. (Chantilly, VA: Mineralogical Society of America), 219

Wong, M. H., Mahaffy, P. R., Atreya, S. K., Niemann, H. B., & Owen, T. C. 2004b, Icar, 171, 153